LANGMUIR

pubs.acs.org/Langmuir Article

Room Temperature Electrochemical-Shock Synthesis of Solid-Solution Medium-Entropy Alloy Nanoparticles for Hydrogen Evolution

Joshua Reyes-Morales,[⊥] Saptarshi Paul,[⊥] Michael Vullo,[⊥] Myles Quinn Edwards, and Jeffrey E. Dick*

Cite This: *Langmuir* 2024, 40, 24272−24280 Read Online

ACCESS | Metrics & More | Article Recommendations | Supporting Information

ABSTRACT: For millennia, humankind has discovered great benefits in alloying materials. Over the past 100 years, a renaissance in nanoscience has cemented the importance of nanoparticles in a variety of fields ranging from energy storage and conversion to cell biology. While many synthetic strategies exist for nanoparticle and alloy nanoparticle formation, new methods are necessary to create nanoparticles under unprecedented conditions. Here, we demonstrate a simple technique to electrodeposit solid-solution alloy nanoparticles at room temperature. When metal salts of platinum, gold, and palladium are confined to nanodroplets suspended in oil, and then a nanodroplet collides with a sufficiently negative-biased electrode to reduce the metal salts at the mass-transfer limitation, solid-solution alloy nanoparticles form. High-angle annular dark-field scanning transmission electron microscopy and single atom energy dispersive X-ray spectroscopy confirm the solid-solution microstructure of the nanoparticles. The results also confirm the nanodroplet's ability to tune alloy microstructures from amorphous to solid-solution. We further extend our technique by adding salts of silver, which lead to the synthesis of polycrystalline medium-entropy alloys. Finally, we go on to show the application of our midentropy alloys toward renewable and clean energy devices by highlighting their electrocatalytic activity toward hydrogen evolution reaction. Our method is unrivaled in its simplicity and will find applications across various fields of study.

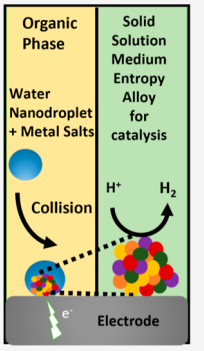

INTRODUCTION

Metal alloys are materials with mixed properties, composed of different elements.[1] The mixing within the alloy can provide enhancement of certain properties like higher heat resistance, durability, stability, etc.[2−4] Historically, alloys are materials that contain more than one element in the material.[5] Different synthetic methods have been used to generate alloy materials, including chemical synthesis,[6] laser ablation,[7] and thermal syntheses.[8,9]

Alloy nanoparticles (NPs), especially those with metals that are in equimolar ratios, are difficult to synthesize because of the disposition of metals to phase separate.[10,11] It must be such that the NPs are kinetically trapped, preventing phase separation. Hu and co-workers developed the carbothermal shock synthesis method where evaporated metals are heated and cooled within milliseconds, forming solid-solution high-entropy alloy NPs.[12] Our group previously introduced a nanodroplet method that takes advantage of rapid mixing within nanodroplets.[13−16] A subfemtoliter droplet can be completely electrolyzed on an electrode in tens of milliseconds.[17] We showed that high-entropy metallic glass NPs can be realized with this method.[14] Several groups took advantage of this method to generate medium- and high-entropy NPs.[18,19] Yet, the nanodroplet method previously reported suffers from many limitations. This is because of the requirement to maintain electroneutrality during the electrodeposition process, and some metal salts would undergo phase-transfer reactions and leave the nanodroplet. Moreover, in the previous study, the potential was held negative enough to drive the reduction of the water nanodroplet itself, causing the precipitation of oxyhydroxides.[14]

Here, we extend our method to demonstrate that the nanodroplet technique can produce solid-solution alloy NPs. We previously showed that we could prevent the phase transfer of complex anions like chloroaurate by a detailed understanding of ion transfer mechanisms during the NP deposition process.[20−22] Nanodroplets were filled with equimolar amounts of chloroplatinate, chloroaurate, and chloropalladate. Upon contact with the carbon electrode, biased sufficiently negative to electroreduce each metal at the mass-transfer limitation without electrolyzing water, solid-solution alloy NPs form.

We further extended this method by adding silver nitrate and lead sulfate to our previous alloy mixture. Hence, we go on to form a polycrystalline midentropy alloy of AuPdPtAgPb. Previously, in the literature, alloys have been classified depending on the number of elements present in the material.

Received: June 24, 2024
Revised: October 8, 2024
Accepted: October 8, 2024
Published: November 9, 2024

https://doi.org/10.1021/acs.langmuir.4c02211
Langmuir 2024, 40, 24272−24280

These can be termed low (fewer than three metals), medium (three to four metals), or high (five or more metals) entropy alloys.[1,23] Also, these alloys can be classified into different groups using the following equation

$$\Delta S = -R \sum_{k=1}^{N} x_k \ln x_k \quad (1)$$

where ΔS is the entropy of mixing, R is the universal gas constant, and x_k is the mole fraction of the particular metal in the alloy. If $\Delta S \leq 0.69$ R, it is a low-entropy alloy, if 1.61 R$\geq \Delta S \geq 0.69$ R, it is a medium-entropy alloy, and if $\Delta S \geq 1.61$ R, it is a high-entropy alloy. Thus, by using this information, we find out which group our AuPdPtAgPb alloy falls in.[24] We found it to be a midentropy system, and we evaluated its electrochemical behavior by performing a hydrogen evolution reaction (HER). HER is at the center of multiple energy storage and conservation systems and is believed to be the future of renewable energy.[25] Therefore, we go on to show that not only is our electrochemical-shock synthesis effective in producing solid-solution alloys at room temperature but also finds several applications.

The uniqueness of this work is seen in the production of polycrystalline solid-solution alloys at room temperature. Generally, most techniques to synthesize polycrystalline alloy NPs include high temperature. Methods like thermal reduction,[26] sol−gel,[27] chemical vapor deposition,[28] and physical vapor deposition[29] to generate polycrystalline alloy NPs have all used significantly higher temperatures than room temperature. Here, using nanodroplet-mediated electrodeposition, we generated polycrystalline solid-solution alloys at room temperature.

The significance of nanodroplet-mediated electrodeposition is seen from these results. Using the advantage of its fast mass transfer (the contents in a femtoliter droplet could be electrolyzed in a few milliseconds),[15] we were not only able to get alloys, which were homogeneous (solid-solution) but also showed a polycrystalline microstructure at room temperature. This is also a clear distinction from previous work done by Glasscott[14] using nanodroplets, where they were able to achieve only amorphous alloys.

Moreover, we go on to show the significance of these alloys in the field of catalysis by demonstrating the HER. All of the elements in the alloy were chosen based on their individual previous performance to HER. As we generate a polycrystalline solid-solution alloy of all of them together, we see a statistically significant response to HER as that of only Pt NPs, but via using only 1/5th the amount of Pt. Thus, bringing down the cost of the catalyst significantly. Therefore, our study not only shows the power of nanodroplet-mediated electrodeposition in generating polycrystalline solid-solution alloys at room temperature but also its significant use in the field of catalysis.

EXPERIMENTAL PROCEDURES

Materials. The chemicals gold chloride(III) hydrate (auric acid; 99.995% trace metal basis), lithium perchlorate (battery grade, 99.99% trace metal basis), potassium tetrachloropalladate (98%), hexachloroplatinic acid (8% w/v stock solution), lead sulfate (98%), and silver nitrate (99.99% trace metal basis) were obtained from Sigma-Aldrich. The organic phase 1,2-dichloroethane (99.8%) was obtained from Sigma-Aldrich. Sulfuric acid (92.25%) was purchased from Fisher Scientific. A highly oriented pyrolytic graphite (HOPG) substrate was obtained from Momentive Performance Materials Quartz, Inc. The cleaning process of the HOPG consisted of using adhesive tape to remove individual layers for exposing new, cleaner layers between different experiments. A 10 μm diameter Pt ultramicroelectrode and Ag/AgCl reference electrodes were purchased from CH Instruments, Austin, Texas. A glassy carbon rod was used as the counter electrode.

Preparation of Solutions. An aqueous solution of 20 mM gold chloride(III) hydrate, 20 mM tetrachloropalladate, 20 mM hexachloroplatinic acid, and 0.25 M $LiClO_4$ in water was prepared. Water-in-oil emulsions were prepared by adding 25 μL of the aqueous solution to 5 mL of 1,2-dichloroethane in a 10 mL fluorinated ethylene propylene tube. The fluorinated ethylene propylene tube was purchased from Oak Ridge Centrifuge Tube from Thermo Scientific. The water used was nanopure water (18.2 MΩ·cm).

Instrumentation. A Pt ultramicroelectrode was used as the working electrode for the collision experiments. A polytetrafluoroethylene cell was used as the electrochemical cell and as the setup for the working electrode. The working electrode was HOPG. A 2 mm diameter Viton O-ring was used to expose the 2 mm diameter of the HOPG working electrode. A Ag/AgCl, which was stored in a solution of 1 M KCl with a salt bridge, was used as the reference electrode. A glassy carbon rod was used as the counter electrode. A Q500 ultrasonic processor (500 W; Qsonica, Newtown, CT) with a microtip probe was used to prepare the water-in-oil emulsions. By applying an amplitude of 40% with a turn on and off for 5 s each for a total of 1 min. The electrochemical technique, chronoamperometry, was used to electrodeposit the NPs with a CHI model 601D potentiostat (CH Instruments, Austin, Texas), where the polarographic convention (Texas) was used. FEI Quanta 3D FEG Dual Beam scanning electron microscopy (SEM) and energy dispersive X-ray spectroscopy (EDX) were used to obtain images of the samples and to confirm the elements present. The voltages used during SEM and EDX were 5 and 10 keV, respectively. A FEI Tecnai G2 20 transmission electron Microscope (TEM) at 200 keV was used to obtain the diffraction pattern of single NPs by using selected area diffraction. A Thermo Scientific Themis Z Double Aberration Corrected S/TEM instrument was used to obtain the dark field images and the EDX mapping of the S/TEM samples. A Pine Research rotating disk electrode (1600 rpm) was used to account for the electrocatalytic behavior of the deposited sample for the HER.

Electrode Preparation. NPs were deposited via amperometry using a PTFE cell with a 2 mm diameter Viton O-ring, where the HOPG had an exposed diameter of 2 mm. The HOPG surface was exfoliated between experiments using adhesive tape to take out individual layers for exposing new cleaner layers. The glassy carbon macroelectrode (not the HOPG) was polished using three different polishing cloths containing 1 μm alumina powder (CH Instruments), 0.3 μm alumina powder (CH Instruments), and a polishing cloth with MQ water, respectively. Commercial Pt microelectrodes were bought from CH Instruments.

Preparation of TEM Samples. To prepare the TEM samples, solutions similar to those mentioned were prepared; however, the working electrode was the TEM grid. To make the electrical connection for the TEM grid, a reverse tweezer was used. The tweezer was used to hold the TEM grid. Then, the working electrode clamp was connected directly to the reverse tweezer. The reverse tweezer tip (with the TEM grid) was submerged into the emulsion for the electrodeposition of the NPs to proceed. After the electrodeposition, the TEM grid was rinsed with MQ water for 1 min and then with acetone for another minute to remove any salt. PELCO TEM grid with support film of carbon on 200 mesh Mo grid was bought from TED PELLA.

Electrocatalytic Properties. To measure the electrocatalytic properties of our synthesized AuPdPtAgPb alloy, we first calculated the electrochemically active surface area (ECSA). We can calculate the ECSA by the following formula: ECSA = C_{dl}/C_s, where C_{dl} is the double layer capacitance and C_s is the specific capacitance of the material. The calculation of C_{dl} can be found in Figure S13. We used 1 M H_2SO_4 to measure the HER activity. Cs obtained from the literature was 0.000035 F/cm^2. Subsequently, ECSA was calculated for our synthesized midentropy alloys, Pt NPs, and our glassy carbon

https://doi.org/10.1021/acs.langmuir.4c02211
Langmuir 2024, 40, 24272−24280

electrode as our control. The calculated ECSA was 0.06249, 0.06206, and 0.09154 cm^2 for our synthesized Pt, midentropy, and glassy carbon electrodes, respectively. These ECSA values were used to calculate the current density. Current density vs potential (at 0.01 V/s) was plotted to estimate the overpotential values.

RESULTS AND DISCUSSION

Schematic of Electrodeposition Process and Droplet Size Analysis. A water-in-oil emulsion was used for the electrodeposition of the NPs. Figure 1 shows a schematic

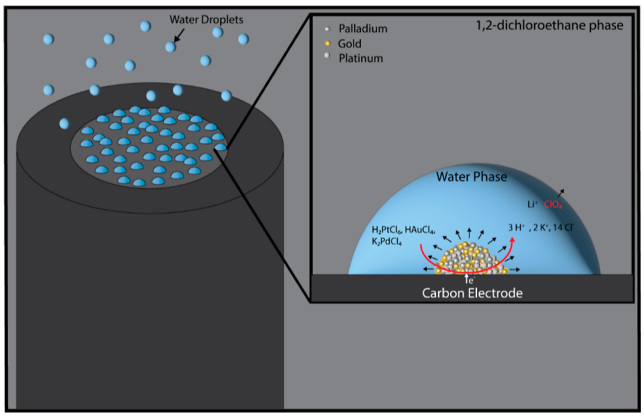

Figure 1. Schematic representation of water droplets suspended in 1,2-dichloroethane. Droplets collide stochastically with the surface of the carbon electrode. After applying a negative potential, metal salts will start to be reduced to generate the AuPdPt solid-solution alloy. To maintain charge balance, ClO_4^- will transfer from the water phase into the 1,2-dichloroethane phase. Inside the water droplets, there are 20 mM $HAuCl_4$, 20 mM K_2PdCl_4, 20 mM H_2PtCl_6, and 0.25 M $LiClO_4$.

representing the synthesis of the alloy nanomaterials. Each droplet was filled with a 60 mM total metal salt concentration (20 mM $HAuCl_4$, 20 mM $PdCl_4$, and 20 mM H_2PtCl_6) with 0.25 M $LiClO_4$. The water droplets containing the metal salts were suspended in 1,2-dichloroethane. With time, droplets stochastically collide with the surface of the electrode. Once a negative potential higher than that of each metals' formal potential is applied, reduction occurs and NPs are formed. During this process, the charge balance must be maintained. Therefore, ClO_4^- will leave the droplet-based on the Gibbs free energy of the anion.[21] Other ions are unlikely and unfavorable to transfer under the experimental conditions because they are more hydrophilic. Previous experiments have shown almost no transfer of these ions.[20,21] This technique of nanodroplet-mediated electrodeposition offers several advantages, including fast electrosynthesis, homogeneity of metals in a single NP, and organized crystal structure.

Figure 2 shows representative chronoamperograms, shown in blue, at 0.3 V versus Ag/AgCl to allow for the complete electrolysis of all the metals. The control experiment, shown in black, shows no reactions happening in the background. Therefore, the collision events observed are due to the reduction of metal salts in the water droplet. For this experiment, an ultramicroelectrode is used since macroelectrodes have a higher capacitance that will not permit the detection of these single individual droplets. During this experiment, a spike response can be observed. Each spike represents a droplet diffusing and colliding with the surface of the electrode, resulting in the species inside the droplets being

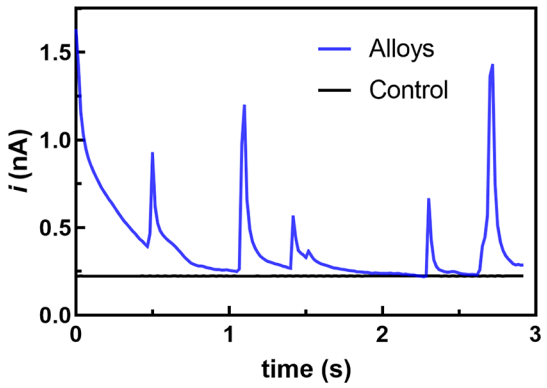

Figure 2. Representative collision experiments of water droplets suspended in 1,2-dichloroethane using a Pt ultramicroelectrode as the working electrode. Water droplets are filled with 20 mM $HAuCl_4$, 20 mM $PdCl_4$, 20 mM H_2PtCl_6, and 0.25 M $LiClO_4$. Chronoamperogram of the control experiment (shown in black) shows water droplets suspended in 1,2-dichloroethane using a Pt ultramicroelectrode. Here, water droplets are filled with HCl and 0.25 M $LiClO_4$. HCl was added accordingly to account for the pH in the droplets containing the metal salt. Applied potential was -0.3 V vs Ag/AgCl. Polarographic convention is used so that the cathodic current is positive.

electrolyzed. The initial increase in current and exponential decay is due to the electrolysis of the metals in the nanodroplet. Using Faraday's Law, the droplet size can be calculated

$$r_{\text{droplet}} = \sqrt[3]{\frac{0.75Q}{\pi nFC}} \quad (2)$$

Equation 2 relates the charge passed during a collision event with the concentration of the redox molecules, the number of electrons transferred, and other constant variables to calculate the radius of a single droplet. Q is the charge integrated under an individual spike, n is the number of electrons transferred, F is Faraday's constant, and C is the total concentration of metal salts. The average radius of water droplets was 580 ± 140 nm. It should be noted from these chronoamperograms that to obtain a single NP it only takes 10 s of milliseconds, and this is where we define the name electrochemical-shock. Not only does this show that a metal NP can be synthesized in less than a second, but it also shows that even a small amount of supporting electrolyte in the water phase enables the electron transfer between the electrode-water interface.

AuPdPt Alloy Nanoparticle Characterization. Electrodeposition of the NPs was done on a HOPG macroelectrode by using chronoamperometry (Figure S1) at -0.4 V vs Ag/AgCl for 240 s. The reason behind performing these experiments for 240 s was to let enough droplets collide with the surface of the electrode. It is important to note that it takes only milliseconds to obtain single NPs; however, droplets collide stochastically, so a time longer than milliseconds is needed to obtain a higher surface coverage. The average size (diameter) distribution of the NPs was 218 nm (Figure S2).

The structure of NPs can be observed in Figure 3a, where particles look spherical, as was previously explained.[21] More particles can be observed in Figure S3, showing that on average, the NPs are spherical. Additionally, EDX was performed, confirming the presence of Au, Pd, and Pt in each NP (Figure S3). On top of that, EDX mapping (Figure 3b) shows a homogeneous distribution of the metals across the

https://doi.org/10.1021/acs.langmuir.4c02211
Langmuir 2024, 40, 24272−24280

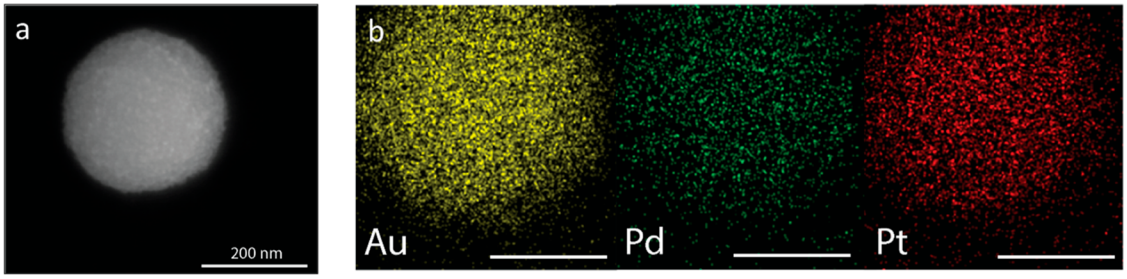

Figure 3. (a) SEM Image of representative nanoparticle (NP) morphology. (b) EDX mapping of each metal is shown (representative scale bar of 100 nm).

NP. A plot of the ratio of metals in each NP is observed in Figure S4. The calculated entropy number was 0.66 R, which is below 0.69 R. This indicates that the synthesized solid-solution NPs are low-entropy alloys. Moreover, the difference in the ratio can be explained based on the kinetics of the electroreduction of the metals. The reduction of gold is more favorable than Pd and Pt.[30] Therefore, applying -0.4 V vs Ag/AgCl results in more favorable electrodeposition of gold over the other metals, which results in lowering the kinetics for the other metal electrodeposition.[31−34] To study the crystallinity of NPs, SEM alone cannot be used. Therefore, we decided to use TEM to study the crystal structure of single NPs (Figure 4).

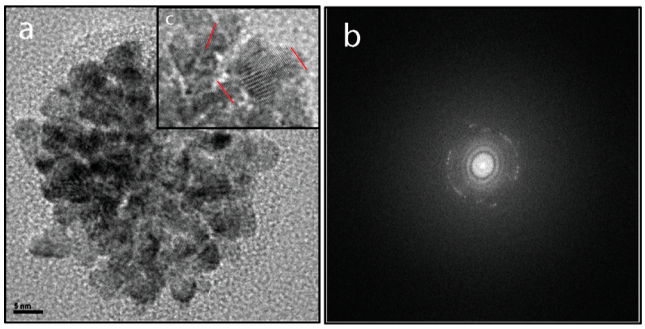

Figure 4. TEM images of a single AuPdPt alloy NP. (a) Shows a bright field image and (b) shows the fast Fourier transform of the TEM bright field image of AuPdPt alloy NP. (c) Shows a close-up of the bright field TEM indicating representative lattice orientation.

Figure 4a shows a TEM image of a single metal alloy. Previously, we electrodeposited high-entropy metallic glass NPs.[14] Percival successfully synthesized crystalline NPs, but the group did not perform the whole experiment at room temperature.[18] They electrodeposited high-entropy alloys via nanodroplet-mediated electrodeposition, which resulted in amorphous NPs. To obtain crystalline materials, they thermally treated the material, resulting in crystalline materials with phase separation. To study crystallinity, the direction of the lattices in a single NP can be observed (Figure 4c). Furthermore, the fast Fourier transform was performed (Figure 4b). The pattern showed clear rings with several bright spots indicating the polycrystallinity of the NP. Therefore, by selecting the appropriate metals and potentials, one can generate NPs with an organized crystal structure.

To confirm the alloys are solid-solutions, high-angle annular dark field scanning TEM was performed (HAADF-STEM) as well as single atom EDX. Previously, several groups have shown single-atom EDX, which exhibits a high resolution toward identifying single atoms with STEM images.[35] Here, we show the use of single-atom EDX to determine the presence of solid-solution alloys (Figure 5b). It can be observed that there is a homogeneous distribution, and no obvious segregation is observed, indicating that the elements are mixed and not phase separated (Figure 5b). Furthermore, a line scan EDX of one of the lines (white line in Figure 5c) was performed. For the line scan, only Pd and gold were compared due to the difficulty when analyzing gold and Pt since the EDX spectra peaks overlap. Figure 5d shows a black curve in which each peak represents the location of the atoms in the line selected with the line scan (Figure 5c). It can be observed that several of the peaks for Pd (red) and gold (green color) match the peaks in the black curve (Figure 5d), an indication that the elements are not phase separated but they are mixed, indicating solid-solution alloys.

Synthesis of Medium-Entropy Alloys. In our previous discussion, we successfully electrodeposited a AuPdPt solid-solution alloy from aqueous nanodroplets. Previous literature has reported on the advantages of alloying for various applications,[2−4,36] especially in the field of catalysis.[37,38] We thus extend the same water-in-oil emulsion system to electrodeposit AuPdPtAgPb alloy and evaluate its electrocatalytic activity toward the HER. Pb and Ag have both been reported previously for their application toward HER.[39−42] The electrodeposition process is similar to that shown in Figure 1. Here, each droplet was filled with a 3 mM concentration of each metal salt (3 mM $HAuCl_4$, 3 mM $PdCl_2$, 3 mM H_2PtCl_6, 3 mM $AgNO_3$, and 3 mM $PbSO_4$) and 0.25 M $LiClO_4$. These droplets were suspended in 1,2-dichloroethane. Collision experiments were performed (Figure S5) to calculate the size of the droplets using eq 2. The size of the droplets was calculated to be 800 ± 200 nm. As time proceeds, the droplets collide with the glassy carbon electrode biased at a negative potential, which drives the reduction of metal salts and the subsequent formation of the NPs. The electrodeposition process was carried out at -0.6 V vs Ag/AgCl for 240 s by using chronoamperometry (Figure S6).

Figure 6a,b shows the SEM and TEM images of the electrodeposited NPs, respectively. As seen from the micrographs, the particles are spherical in shape. The average size of the NPs was calculated to be 230 nm (Figure S7). EDX was performed, showing the presence of Au, Pd, Pt, Ag, and Pb in the NPs (Figures S8 and S9). Note should be taken that the EDX spectra peaks for Au and Pt overlap with one another. Additionally, Figure 6c shows a HAADF-STEM image of the AuPdPtAgPb alloy with accompanying high-resolution EDX images showing the elemental distribution of the metals and an EDX overlay of all of the metals. The configurational entropy presented in eq 1 can be calculated by using the fraction of

https://doi.org/10.1021/acs.langmuir.4c02211
Langmuir 2024, 40, 24272−24280

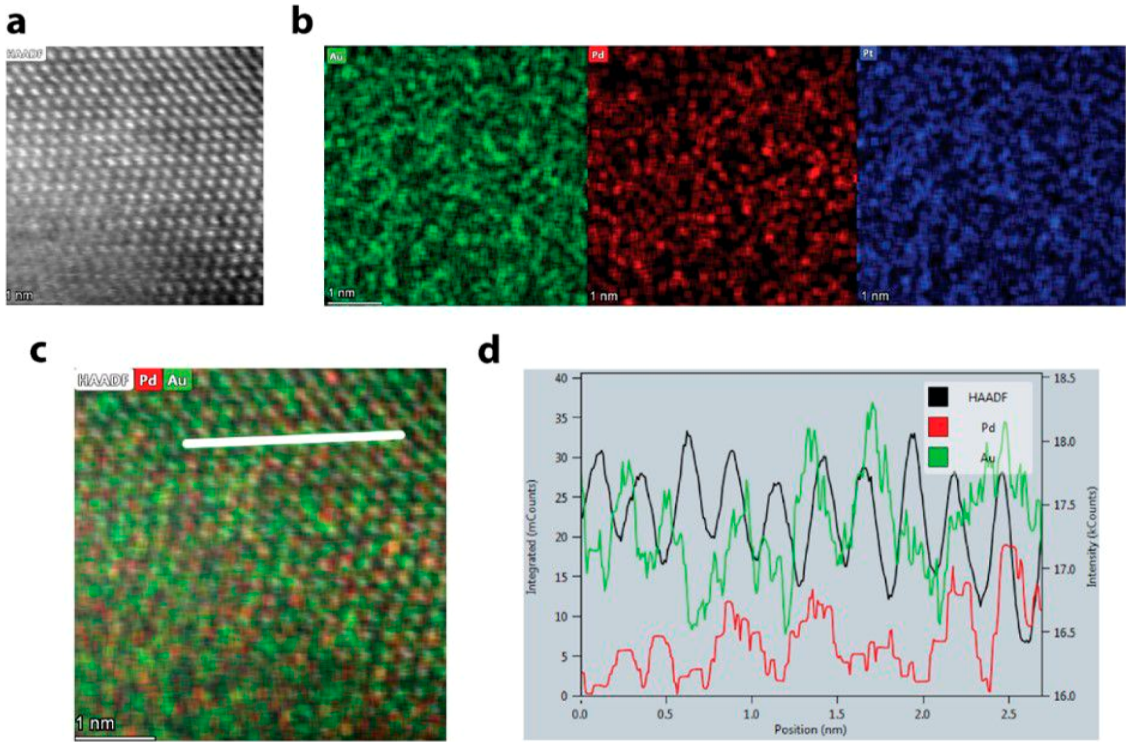

Figure 5. STEM of solid-solution alloys. (a) High-angle annular dark field image of an AuPdPt alloy showing individual atoms in the particle. (b) EDX of the particle showing a homogeneous distribution of the metals in the alloy NP. (c) EDX mapping overlay of gold and palladium. (d) EDX line scan showing the location of the metal atoms in a selected part of the particle. White line in c is where the EDX line scan was performed.

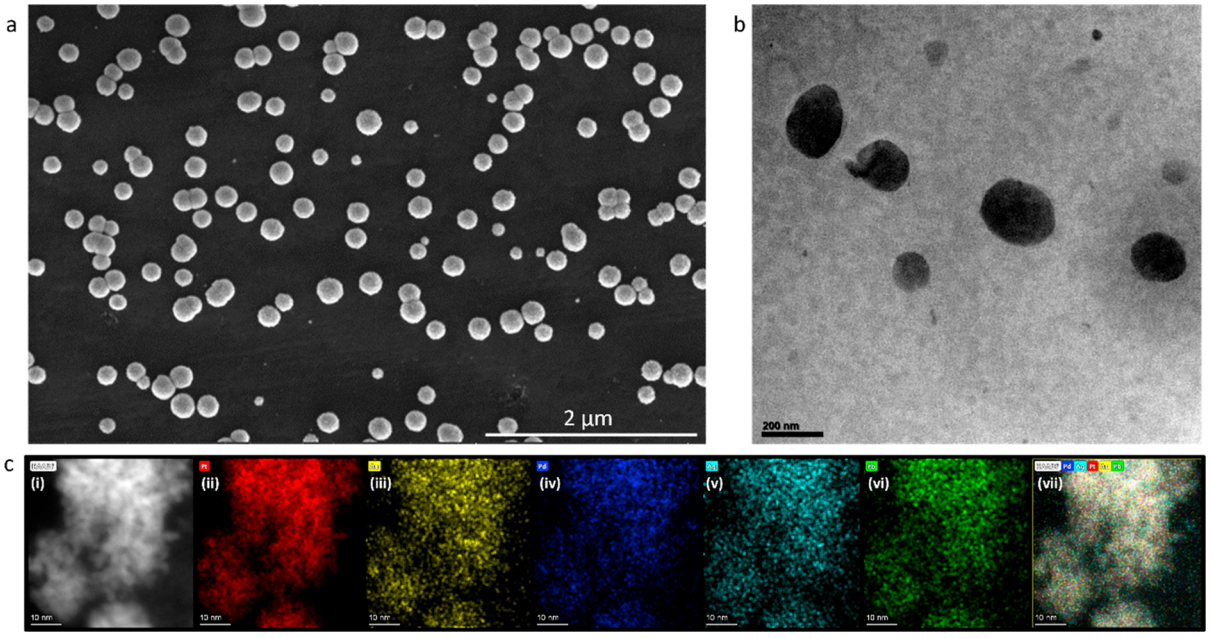

Figure 6. (a) SEM image of deposited AuPdPtAgPb alloy NPs. (b) TEM image (bright field) of deposited alloy NPs. (c)STEM of our deposited alloy NPs. (i)STEM-HAADF image of alloy NPs. (ii–vi) Represent the EDX mapping of Pt, Au, Pd, Ag, and Pb, respectively. (vii) Represents an overlay of all the elements. Scale bar is 10 nm for all the images shown in (c).

each element. The calculated entropy number was 1.42 R, which is above 0.69 R and below 1.61 R indicating that the synthesized NPs are midentropy alloys.[23] The entropy of both AuPdPt and AuPdPtAgPb alloys was calculated from their datasets of elemental composition, and it was found out to be 0.66 R ± 0.02 and 1.42 R ± 0.03 R, respectively. Multiple SEM–EDX datasets of both AuPdPt and AuAgPdPbPt were taken to get an estimate of each element present in the alloy. SEM–EDX data with their elemental composition is provided in Figures S10 and S11.

Figure 7a (inset) shows the TEM image of a single metal alloy. The close-up picture shows the direction of the lattices. The different directions of the lattices in the single NP indicate the polycrystallinity of the material. In Figure 7b, the fast

https://doi.org/10.1021/acs.langmuir.4c02211
Langmuir 2024, 40, 24272–24280

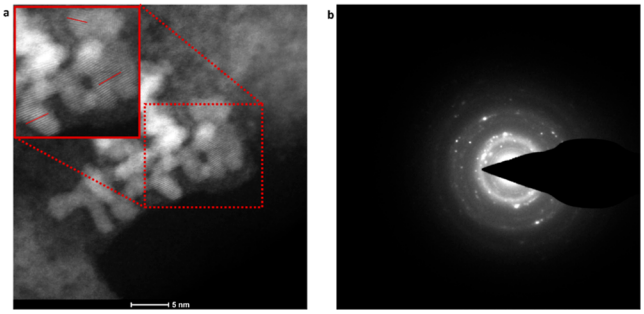

Figure 7. TEM images of a single AuPdPtAgPb alloy NP. (a) Depicts a dark field image and an inset demonstrating different lattice directions. (b) SAED of our deposited NPs.

Fourier transform was performed using selected area electron diffraction (SAED), and rings with many bright spots were seen, indicating the polycrystallinity of the NP. These data show the polycrystalline nature of our synthesized medium-entropy alloys.

Here, it is also important to note how different parameters affect the electrodeposition of the alloys and how the size, composition, and shape of the NP be tuned. The size of the NPs formed is related to the size of the droplets, as pointed out by Glasscott.[43] The sizes of AuPdPt alloys are smaller than those of AuPdPtAgPb alloy. This is possible due to the higher size of droplets observed in the case for AuPdPtAgPb compared to that of AuPdPt. As upon collision with the electrode, AuPdPtAgPb droplets get a higher contact surface area to deposit, and due to the fast mass transfer process, a larger size of the NP alloy is observed.

The composition of the alloys formed is directly related to the potential applied. The onset deposition potentials for different elements are different, which inherently affects the composition of the alloys formed. Also, a higher precursor concentration of an element would result in more coverage of that element in the alloy.

The shape of the electrodeposited NP can also be tuned in different ways. Previous reports have shown how changing the electrolyte (from TBAP to $LiClO_4$) can result in different shapes.[21] Along with that, using a surfactant or changing the concentration of the precursor element can also result in the change of its shape (from uniform to more dendritic).[43,44]

Application to the Hydrogen Evolution Reaction. As discussed previously, HER is at the center of renewable and clean energy devices.[45] Various metals, including Au, Ag, Pb, and Pd, have been the subject of prior investigations regarding their involvement in HER.[46−49] Nonetheless, Pt remains the preeminent catalyst for HER,[39] despite its considerable market cost. In light of this, our research aims to discern the electrocatalytic efficacy of our synthesized midentropy alloy, AuPdPtAgPb, in comparison to Pt NPs with respect to HER.

We chose to evaluate our midentropy electrocatalyst for HER in 1 M H_2SO_4. We deposited our midentropy alloy system of AuPdPtAgPb on a glassy carbon rotating disc electrode. We then determined the ECSA of our deposited sample to calculate the current density. To do this, we calculated the double-layer capacitance of our catalyst in a nonfaradaic region (Figure S13). This double-layer capacitance can be correlated with the ECSA by using the specific capacitance of the material; details of this process are given in the Experimental Procedures section.

Using the above process, we also evaluated the HER electrocatalytic behavior for a glassy carbon electrode with Pt NPs. We electrodeposited Pt NPs on the glassy carbon electrode using the same water-in-oil emulsion system, as discussed in Figure 1. We used the same solution (1 M H_2SO_4) to see its electrocatalytic behavior and to calculate its ECSA and current density in the same process as that discussed above. The SEM and EDX of the deposited Pt NPs were done and are provided in Figure S12. The average size of the NPs was found to be around 298 nm.

The ECSA of Pt and AuPdPtAgPb alloys was calculated to be 0.06249 and 0.06206 cm^2. Thus, they were found to be close to each other. Also, the final current was normalized with respect to the ECSA to get the current density. The overpotential is measured as the potential at which the current density reaches 10 mA/cm^2. This technique of evaluating the catalytic property has been benchmarked by Jaramillo and group.[50] This whole process of calculating ECSA via calculating C_s (specific capacitance) and C_{dl} (double layer capacitance) is given in the Experimental Procedures and Supporting Information.

Figure 8 shows the electrocatalytic activity of our synthesized midentropy alloys (blue), Pt NPs (black), and bare glassy carbon electrode as a control (red). Ten mA/cm^2 is the standard benchmark to calculate overpotential and comment on the electrocatalytic behavior of the material.[51] For HER, the thermodynamic potential is 0 V vs RHE.[15] The calculated overpotential from Figure 8 for Pt NPs was 0.27 V, and for the midentropy alloys, it was 0.28 V. Therefore, midentropy alloys showed no statistical difference in catalytic ability when compared to Pt NPs while using only 1/5th of the Pt that was used to synthesize the Pt NPs. Figure S14 goes on to show the stability of our synthesized midentropy alloy system at hydrogen evolution potential (−0.28 V vs SHE) as our synthesized midentropy alloys maintain constant current for over two hours without any appreciable decay. This goes on to show our synthesized midentropy AuPdPtAgPb alloy is long-lasting and able to preserve its electrochemical behavior throughout the HER.[45]

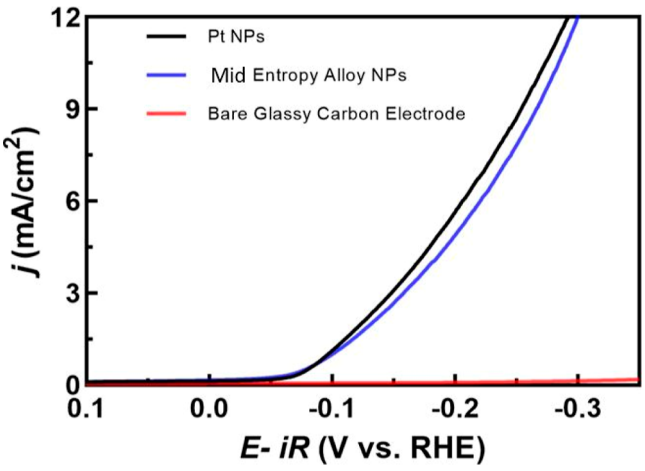

Figure 8. Electrocatalytic activity of AuPdPtAgPb alloy NPs toward HER. Current density vs potential plot for Pt NPs (Pt NPs), midentropy alloy NPs, and bare glassy carbon electrode. ("NPs" in the figure stand for nanoparticles.)

The consistent behavior of the stability curve (Figure S14) for around 2 h hints at the fact that the morphology and the

https://doi.org/10.1021/acs.langmuir.4c02211
Langmuir 2024, 40, 24272−24280

composition of the alloy remained stable over time, as a change in the composition or morphology should affect its catalytic behavior as well. Depending on the potential applied and the precursor concentration of the elements taken, the composition of the alloy may vary, which may also affect the catalytic performance of the alloy. The AuPdPt alloy should also show commendable catalytic property; however, we extended our system to the AuPdPtAgPb alloy in order to have similar catalytic property but in turn use a much lower amount of Pt and thereby reduce the cost of the material significantly.

CONCLUSIONS

Nanodroplet-mediated electrodeposition has been shown to be a versatile technique to generate metal NPs. Here, we show the synthesis of solid-solution alloys at room temperature. STEM with EDX mapping of individual atoms showed a homogeneous distribution of elements in the NP, confirming the synthesis of solid-solution alloys. Moreover, TEM showed the organization of the atoms, resulting in polycrystalline NPs. With the results presented, it is shown that solid-solution nanomaterials can be generated in a simple way at room temperature. Additionally, we go on to show the electrocatalytic activity of our synthesized polycrystalline midentropy alloy by demonstrating the HER. Its electrocatalytic activity is comparable to Pt NPs while using only 1/5th of the Pt. Not only is our method cost-effective, but it also goes on to show its applications in energy storage and clean energy devices.

ASSOCIATED CONTENT

Supporting Information

The Supporting Information is available free of charge at https://pubs.acs.org/doi/10.1021/acs.langmuir.4c02211.

Representative chronoamperogram for the electrodeposition of the alloy systems AuPdPt and AuPdPtAgPb; SEM−EDX, TEM, and statistical analysis for the two alloy systems; and C_{dl} calculation from current vs scan rate plot and stability curve for catalysis (PDF)

AUTHOR INFORMATION

Corresponding Author

Jeffrey E. Dick − *Department of Chemistry, Purdue University, West Lafayette, Indiana 47907, United States; Elmore Family School of Electrical and Computer Engineering, Purdue University, West Lafayette, Indiana 47907, United States;* orcid.org/0000-0002-4538-9705; Email: jdick@purdue.edu

Authors

Joshua Reyes-Morales − *Department of Chemistry, Purdue University, West Lafayette, Indiana 47907, United States; Department of Chemistry, Universidad Ana G. Méndez, Gurabo, Puerto Rico 00778, United States*

Saptarshi Paul − *Department of Chemistry, Purdue University, West Lafayette, Indiana 47907, United States*

Michael Vullo − *Department of Chemistry, SUNY Buffalo State University, Buffalo, New York 14222, United States*

Myles Quinn Edwards − *Department of Chemistry, Purdue University, West Lafayette, Indiana 47907, United States*

Complete contact information is available at: https://pubs.acs.org/10.1021/acs.langmuir.4c02211

Author Contributions

[⊥]J.R.-M., S.P., and M.V. contributed equally to this work. J.R.M., S.P., and J.E.D. wrote the manuscript with M.Q.E. providing edits. The concept of the nanodroplet-mediated solid-solution medium-entropy alloy formation and its subsequent impact on HER enhancement was conceived by J.R.M., S.P., M.V., and J.E.D. All the electrochemical experiments were done by J.R.M., S.P., and M.V. All the electronic microscopic characterizations were done by J.R.M. and S.P. The catalysis experiments were done by M.V. M.Q.E. helped in electrochemical experiments and analysis of NPs from microscopic data to have a size distribution histogram. J.R.M., S.P., M.V., M.Q.E., and J.E.D. helped in the interpretation of the data. J.E.D. supervised all aspects of the work. All authors have approved the final version of the manuscript.

Notes

The authors declare no competing financial interest.

ACKNOWLEDGMENTS

The authors would like to acknowledge the use of facilities within the Purdue Electron Microscopy Center. Facility RRID SCR_022687. We would like to acknowledge Dr. Christopher Gilpin and Dr. Zhongxia Shang from the Purdue Electron Microscopy Center. We acknowledge the support by the National Science Foundation CAREER under grant no. CHE-2045672. ChatGPT was used only for checking grammar.

REFERENCES

(1) Gao, S.; Hao, S.; Huang, Z.; Yuan, Y.; Han, S.; Lei, L.; Zhang, X.; Shahbazian-Yassar, R.; Lu, J. Synthesis of high-entropy alloy nanoparticles on supports by the fast moving bed pyrolysis. *Nat. Commun.* **2020**, *11* (1), 2016.

(2) Dan, A.; Cojocaru, E. M.; Raducanu, D.; Cinca, I.; Cojocaru, V. D.; Galbinasu, B. M. Microstructure and mechanical properties evolution during thermomechanical processing of a Ti−Nb−Zr−Ta−Sn−Fe alloy. *J. Mater. Res. Technol.* **2022**, *19*, 2877−2887.

(3) Jawed, S. F.; Rabadia, C. D.; Khan, M. A.; Khan, S. J. Effect of Alloying Elements on the Compressive Mechanical Properties of Biomedical Titanium Alloys: A Systematic Review. *ACS Omega* **2022**, *7* (34), 29526−29542.

(4) Orłowska, M.; Ura-Bińczyk, E.; Śnieżek, L.; Skudniewski, P.; Kulczyk, M.; Adamczyk-Cieślak, B.; Mizera, J. Increasing the Mechanical Strength and Corrosion Resistance of Aluminum Alloy 7075 via Hydrostatic Extrusion and Aging. *Materials* **2022**, *15* (13), 4577.

(5) Cao, F.; Munroe, P.; Zhou, Z.; Xie, Z. Medium entropy alloy CoCrNi coatings: Enhancing hardness and damage-tolerance through a nanotwinned structuring. *Surf. Coat. Technol.* **2018**, *335*, 257−264.

(6) Huynh, K.-H.; Pham, X.-H.; Kim, J.; Lee, S. H.; Chang, H.; Rho, W.-Y.; Jun, B.-H. Synthesis, properties, and biological applications of metallic alloy nanoparticles. *Int. J. Mol. Sci.* **2020**, *21* (14), 5174.

(7) Neumeister, A.; Jakobi, J.; Rehbock, C.; Moysig, J.; Barcikowski, S. Monophasic ligand-free alloy nanoparticle synthesis determinants during pulsed laser ablation of bulk alloy and consolidated microparticles in water. *Phys. Chem. Chem. Phys.* **2014**, *16* (43), 23671−23678.

(8) Das, S. K.; Das, A.; Gaboardi, M.; Pollastri, S.; Dhamale, G. D.; Balasubramanian, C.; Joseph, B. Large scale synthesis of copper nickel alloy nanoparticles with reduced compressibility using arc thermal plasma process. *Sci. Rep.* **2021**, *11* (1), 7629.

(9) He, S.; Liu, Y.; Zhan, H.; Guan, L. Direct Thermal Annealing Synthesis of Ordered Pt Alloy Nanoparticles Coated with a Thin N-Doped Carbon Shell for the Oxygen Reduction Reaction. *ACS Catal.* **2021**, *11* (15), 9355−9365.

(10) Yao, Y.; Huang, Z.; Hughes, L. A.; Gao, J.; Li, T.; Morris, D.; Zeltmann, S. E.; Savitzky, B. H.; Ophus, C.; Finfrock, Y. Z.; et al. Extreme mixing in nanoscale transition metal alloys. *Matter* **2021**, *4* (7), 2340−2353.
(11) de Oliveira, P. F. M.; Torresi, R. M.; Emmerling, F.; Camargo, P. H. C. Challenges and opportunities in the bottom-up mechanochemical synthesis of noble metal nanoparticles. *J. Mater. Chem. A* **2020**, *8* (32), 16114−16141.
(12) Yao, Y.; Huang, Z.; Xie, P.; Lacey, S. D.; Jacob, R. J.; Xie, H.; Chen, F.; Nie, A.; Pu, T.; Rehwoldt, M.; et al. Carbothermal shock synthesis of high-entropy-alloy nanoparticles. *Science* **2018**, *359* (6383), 1489−1494.
(13) Tarolla, N. E.; Voci, S.; Reyes-Morales, J.; Pendergast, A. D.; Dick, J. E. Electrodeposition of ligand-free copper nanoparticles from aqueous nanodroplets. *J. Mater. Chem. A* **2021**, *9* (35), 20048−20057.
(14) Glasscott, M. W.; Pendergast, A. D.; Goines, S.; Bishop, A. R.; Hoang, A. T.; Renault, C.; Dick, J. E. Electrosynthesis of high-entropy metallic glass nanoparticles for designer, multi-functional electrocatalysis. *Nat. Commun.* **2019**, *10* (1), 2650.
(15) Reyes-Morales, J.; Dick, J. E. Electrochemical-Shock Synthesis of Nanoparticles from Sub-femtoliter Nanodroplets. *Acc. Chem. Res.* **2023**, *56* (10), 1178−1189.
(16) Paul, S.; Reyes-Morales, J.; Roy, K.; Dick, J. E. Anodic Electrodeposition of IrO_x Nanoparticles from Aqueous Nanodroplets. *ACS Nanosci. Au* **2024**, *4* (3), 216−222.
(17) Jeun, Y. E.; Park, J. H.; Kim, J. Y.; Ahn, H. S. Stoichiometry-Controlled Synthesis of Nanoparticulate Mixed-Metal Oxyhydroxide Oxygen Evolving Catalysts by Electrochemistry in Aqueous Nanodroplets. *Chem.—Eur. J.* **2020**, *26* (18), 4039−4043.
(18) Percival, S. J.; Lu, P.; Lowry, D. R.; Nenoff, T. M. Electrodeposition of Complex High Entropy Oxides via Water Droplet Formation and Conversion to Crystalline Alloy Nanoparticles. *Langmuir* **2022**, *38* (5), 1923−1928.
(19) Murakami, Y.; Murase, K.; Fukami, K. Smooth Thin Film of a CoNiCu Medium-Entropy Alloy Consisting of Single Nanometer-Sized Grains Formed by Electrodeposition in a Water-in-Oil Emulsion. *J. Phys. Chem. C* **2023**, *127* (9), 4696−4703.
(20) Reyes-Morales, J.; Moazeb, M.; Colón-Quintana, G. S.; Dick, J. E. The electrodeposition of gold nanoparticles from aqueous nanodroplets. *Chem. Commun.* **2022**, *58* (76), 10663−10666.
(21) Reyes-Morales, J.; Vanderkwaak, B. T.; Dick, J. E. Enabling practical nanoparticle electrodeposition from aqueous nanodroplets. *Nanoscale* **2022**, *14* (7), 2750−2757.
(22) Colón-Quintana, G. S.; Clarke, T. B.; Dick, J. E. Interfacial solute flux promotes emulsification at the water|oil interface. *Nat. Commun.* **2023**, *14*, 705.
(23) Glasscott, M. W. Classifying and benchmarking high-entropy alloys and associated materials for electrocatalysis: A brief review of best practices. *Curr. Opin. Electrochem.* **2022**, *34*, 100976.
(24) Yeh, J. W. Recent progress in high entropy alloys. *Ann. Chimie Sci. Matériaux* **2006**, *31* (6), 633−648.
(25) Eftekhari, A. Electrocatalysts for hydrogen evolution reaction. *Int. J. Hydrogen Energy* **2017**, *42* (16), 11053−11077.
(26) Ma, D. W.; Cheng, C. Preparations and characterizations of polycrystalline PbSe thin films by a thermal reduction method. *J. Alloys Compd.* **2011**, *509* (23), 6595−6598.
(27) Vinogradov, A. V.; Vinogradov, V. V. Low-temperature sol−gel synthesis of crystalline materials. *RSC Adv.* **2014**, *4* (86), 45903−45919.
(28) Askari, S. J.; Chen, G. C.; Lu, F. X. Growth of polycrystalline and nanocrystalline diamond films on pure titanium by microwave plasma assisted CVD process. *Mater. Res. Bull.* **2008**, *43* (5), 1086−1092.
(29) Garcés, G.; Cristina, M. C.; Torralba, M.; Adeva, P. Texture of magnesium alloy films growth by physical vapour deposition (PVD). *J. Alloys Compd.* **2000**, *309* (1−2), 229−238.
(30) Bard, A. J.; Faulkner, L. R. Electrochemical Methods: Fundamentals and Applications. *Russ. J. Electrochem.* **2002**, *38*, 1364−1365 Wiley, New York, 2001, 2nd ed..
(31) Palomar-Pardavé, M.; González, I.; Batina, N. New Insights into Evaluation of Kinetic Parameters for Potentiostatic Metal Deposition with Underpotential and Overpotential Deposition Processes. *J. Phys. Chem. B* **2000**, *104* (15), 3545−3555.
(32) Stoychev, D.; Papoutsis, A.; Kelaidopoulou, A.; Kokkinidis, G.; Milchev, A. Electrodeposition of platinum on metallic and non-metallic substrates — selection of experimental conditions. *Mater. Chem. Phys.* **2001**, *72* (3), 360−365.
(33) Dhanasekaran, P.; Rajavarman, S.; Selvaganesh, S. V.; Bhat, S. D. Insight towards Nucleation Mechanism and Change in Morphology for Nanostructured Platinum Thin Film Directly Grown on Carbon Substrate via Electrochemical Deposition. *Materials* **2021**, *14*, 2330.
(34) Ren, X.; An, M. Theoretical and experimental studies of the influence of gold ions and DMH on cyanide-free gold electrodeposition. *RSC Adv.* **2018**, *8* (5), 2667−2677.
(35) Lovejoy, T. C.; Ramasse, Q. M.; Falke, M.; Kaeppel, A.; Terborg, R.; Zan, R.; Dellby, N.; Krivanek, O. L. Single atom identification by energy dispersive x-ray spectroscopy. *Appl. Phys. Lett.* **2012**, *100* (15), 154101.
(36) Otto, F.; Yang, Y.; Bei, H.; George, E. P. Relative effects of enthalpy and entropy on the phase stability of equiatomic high-entropy alloys. *Acta Mater.* **2013**, *61* (7), 2628−2638.
(37) Xin, Y.; Li, S.; Qian, Y.; Zhu, W.; Yuan, H.; Jiang, P.; Guo, R.; Wang, L. High-entropy alloys as a platform for catalysis: progress, challenges, and opportunities. *ACS Catal.* **2020**, *10* (19), 11280−11306.
(38) Kumar Katiyar, N.; Biswas, K.; Yeh, J.-W.; Sharma, S.; Sekhar Tiwary, C. A perspective on the catalysis using the high entropy alloys. *Nano Energy* **2021**, *88*, 106261.
(39) Li, Z.; Fu, J.-Y.; Feng, Y.; Dong, C.-K.; Liu, H.; Du, X.-W. A silver catalyst activated by stacking faults for the hydrogen evolution reaction. *Nat. Catal.* **2019**, *2* (12), 1107−1114.
(40) Rolly, G. S.; Meyerstein, D.; Yardeni, G.; Bar-Ziv, R.; Zidki, T. New insights into HER catalysis: The effect of nano-silica support on catalysis by silver nanoparticles. *Phys. Chem. Chem. Phys.* **2020**, *22* (11), 6401−6405.
(41) Wu, Y. M.; Li, W. S.; Long, X. M.; Wu, F. H.; Chen, H. Y.; Yan, J. H.; Zhang, C. R. Effect of bismuth on hydrogen evolution reaction on lead in sulfuric acid solution. *J. Power Sources* **2005**, *144* (2), 338−345.
(42) Papageorgiou, N.; Skyllas-Kazacos, M. A study of the hydrogen evolution reaction on lead bismuth alloys in sulphuric acid solutions. *Electrochim. Acta* **1992**, *37* (2), 269−276.
(43) Glasscott, M. W.; Pendergast, A. D.; Dick, J. E. A Universal Platform for the Electrodeposition of Ligand-Free Metal Nanoparticles from a Water-in-Oil Emulsion System. *ACS Appl. Nano Mater.* **2018**, *1* (10), 5702−5711.
(44) Pendergast, A. D.; Glasscott, M. W.; Renault, C.; Dick, J. E. One-step electrodeposition of ligand-free PdPt alloy nanoparticles from water droplets: Controlling size, coverage, and elemental stoichiometry. *Electrochem. Commun.* **2019**, *98*, 1−5.
(45) Shilpa, R.; Sibi, K.; Sarath Kumar, S.; Pai, R.; Rakhi, R. Electrocatalysts for Hydrogen Evolution Reaction. *Mater. Hydrogen Prod.* **2023**, 115−146.
(46) Lv, H.; Xi, Z.; Chen, Z.; Guo, S.; Yu, Y.; Zhu, W.; Li, Q.; Zhang, X.; Pan, M.; Lu, G.; et al. A new core/shell NiAu/Au nanoparticle catalyst with Pt-like activity for hydrogen evolution reaction. *J. Am. Chem. Soc.* **2015**, *137* (18), 5859−5862.
(47) Tang, M. H.; Hahn, C.; Klobuchar, A. J.; Ng, J. W. D.; Wellendorff, J.; Bligaard, T.; Jaramillo, T. F. Nickel−silver alloy electrocatalysts for hydrogen evolution and oxidation in an alkaline electrolyte. *Phys. Chem. Chem. Phys.* **2014**, *16* (36), 19250−19257.
(48) Wang, L.; Xiao, H.; Cheng, T.; Li, Y.; Goddard, W. A., III Pb-activated amine-assisted photocatalytic hydrogen evolution reaction on organic−inorganic perovskites. *J. Am. Chem. Soc.* **2018**, *140* (6), 1994−1997.

https://doi.org/10.1021/acs.langmuir.4c02211
Langmuir 2024, 40, 24272−24280

(49) Sarno, M.; Ponticorvo, E. Continuous flow HER and MOR evaluation of a new Pt/Pd/Co nano electrocatalyst. *Appl. Surf. Sci.* **2018**, *459*, 105−113.
(50) McCrory, C. C. L.; Jung, S.; Ferrer, I. M.; Chatman, S. M.; Peters, J. C.; Jaramillo, T. F. Benchmarking Hydrogen Evolving Reaction and Oxygen Evolving Reaction Electrocatalysts for Solar Water Splitting Devices. *J. Am. Chem. Soc.* **2015**, *137* (13), 4347−4357.
(51) Wei, C.; Rao, R. R.; Peng, J.; Huang, B.; Stephens, I. E.; Risch, M.; Xu, Z. J.; Shao-Horn, Y. Recommended practices and benchmark activity for hydrogen and oxygen electrocatalysis in water splitting and fuel cells. *Adv. Mater.* **2019**, *31* (31), 1806296.

https://doi.org/10.1021/acs.langmuir.4c02211
Langmuir 2024, 40, 24272−24280